Supplementary Information for Power et al., 'The Liquid to Solid-Like Behaviour in Metastable States of Single Aerosol Particles'

Simulations of back-scattered light intensity from oscillating aqueous sodium chloride droplets

Following coalescence, droplets undergo deformations whose amplitudes oscillate and decay with time. In the optical tweezers measurements described, the measured light intensity arises from the back scattered intensity integrated over the numerical aperture of the objective lens varying over time as a result of the decaying deformation. In order to simulate, and thereby understand, the measured signal, one would require knowledge of the amplitudes and phases of each of the normal modes comprising the compound oscillation, equation (1) of the main paper.[31-33] It not clear that the backscattered signal can be uniquely inverted to obtain these quantities. Instead, we perform a non-linear least squares fit of a simulated signal to the experimental measurement for the reference system in this work, aqueous sodium chloride, assuming literature values for the surface tension and viscosity. At this stage, our aim is to simply ensure that the physical origin of the time-dependent scattering profiles is well-understood. Then, from the decay time-constants for sucrose and mixed sucrose/sodium chloride droplets, we can have confidence in estimating viscosities from the time-dependent decays of the light scattering intensity.

We must first perform light scattering calculations for particles that can be assumed to be spheroidal in shape with varying degrees of deformation. Incident, scattered and internal fields are expressed as truncated sums over a complete orthogonal set of vector spherical wavefunctions (VSWF). By virtue of the linearity of the scattering process, the expansion coefficients describing the incident field are linearly related to those describing the scattered field via the transition or T-matrix. For axially symmetric particles, such as those considered here, the T-matrix can be evaluated in numerous ways. Here we employ the generalized point matching method (GPMM),[34] but note that the results have been shown to agree with those obtained using the extended boundary condition method (EBCM).[35] We truncate the VSWF sums at a value of $N_{max} = 60$, which satisfies the Wiscombe's condition.[36] The incident radiation has a wavelength of λ_0=532nm and is described by a localized Gaussian beam [37] with a waist radius of $4\lambda_0$ although the backscattered intensity does not qualitatively vary with the waist radius. The direction of propagation is perpendicular to the symmetry axis of the droplet which is, in turn, parallel to the polarization direction. The necessary rotation of the incident beam with respect to the particle is performed via the rotation theorem for VSWF.[35] It is noted that, because of the relative size of the droplet and beam, and the modest deviation from sphericity, the direction of polarization makes little difference to the back scattered intensity. Variations with beam waist radius, and with the position of the droplet in the focussed Gaussian beam are also minor and quantitative, but do not affect the qualitative picture.

We note that the refractive indices of the droplets cover a very small range for the coalescence events studied. Normalizing droplet dimensions according to the wavelength in the particle allows us to accommodate this variation, but ignores the minor changes to the beam waist which occur as a result. These

latter changes may be considered negligible within the range of refractive indices we consider. This allows us, therefore, to use a reduced size parameter, for instance, in Figure 2a.

Following Yamada et al.,[38] we assume that the deformed droplet, whose true shape may be quite complex, can be approximated by a spheroid with degenerate radii, *a* and unique radius *b*. The symmetry axis of the spheroidal droplet is assumed to lie parallel to the line connecting the centres of the two original droplets prior to coalescence i.e. the radius *b* is perpendicular to the beam axis. T-matrix calculations are used to evaluate the integrated backscattered intensity (see below). This quantity is shown as a function of equivalent radius, r_{equiv}, the radius of a sphere of identical volume to the spheroid represented, and deformation parameter, $\delta = a - r_{equiv}$, which measures the droplet distortion in terms of the absolute extension of the droplet radius in the direction of the beam axis.

The strongest variation in the back scattered signal is an oscillation which is approximately periodic in *a*, the spheroid radius in the direction parallel to the beam axis. In this respect it is similar to variations in the reflectivity of a dielectric lamina with an equivalent thickness. [39] Given the relative sizes of the beam and the droplet, this is not an unexpected observation with the beam considerably smaller at waist than the droplet diameter. Departures from the case of the dielectric lamina occur due to the finite size of the droplet, and the convergence of the beam; the maxima are not perfectly periodic nor do they coincide exactly with those of a lamina. Furthermore, the back scattered intensity does not fall to zero, and is not completely determined by the vertical radius. Nevertheless, the dependence on *a* is strong enough to assume that the backscatter is largely insensitive to further details of the shape.

Taking the droplet size and refractive index from the cavity enhanced Raman scattering fingerprint, [40] we use Eq.1 to describe the variation of δ in time. We use the parameterisation of Tang et al. [41] to convert refractive index to sodium chloride concentration, allowing the viscosity to be calculated from Chenlo [42] and the surface tension to be calculated from Aerosol Diameter Dependent Model (ADDEM),[43,44] thereby fixing the decay rate and frequency of each mode. All surface tension predictions are based on empirical fits to bulk phase data. We therefore expect a strong agreement between the predicted and actual values used in the sub-saturated regime as in Figure 2 b). While the surface tension may vary slightly from the predicted value in the super-saturated regime, the error introduced over 12 orders of magnitude in viscosity will be negligible.

The amplitudes and phases of the first three oscillating modes of the droplet are fitted to the experimental data in such a way as to minimize the square error. We note that the experimentally measured intensity is normalized to the interval [0,1] and that, for any particular set of amplitudes and phases, the simulated trace is similarly rescaled prior to evaluation of the error.

As can be seen from figure 2b, the measurement can be well approximated, for late times, by a superposition of the first three modes, when the backscatter is approximated as described above. It should be noted that the flat troughs of the signal correspond to regions where these modes interfere destructively. Any perturbation of the fitting parameters spoils this relationship, and new features, not appearing in the optimal fit and experiment, appear. Figure S1 illustrates this, showing the sensitivity in the simulated signal when the radius,

viscosity and surface tension are varied. Given the sensitivity of the signal to the radius of the droplet, the importance of an accurate determination of radius is clearly apparent and is a unique benefit of the spectroscopic CERS technique applied here.

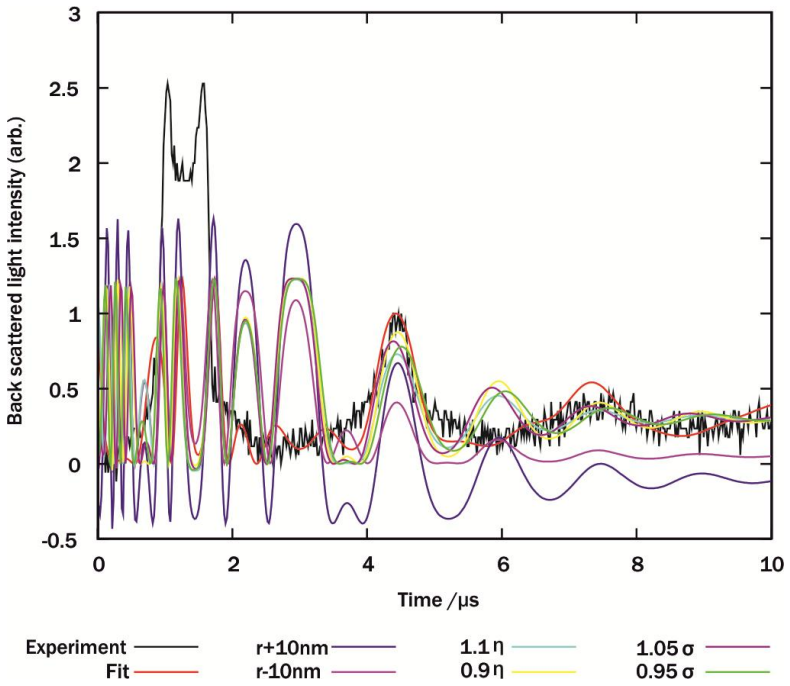

Figure S1: Illustration of the sensitivity of the fitted light scattering signal to variation in the radius, viscosity and surface tension of the droplet

A recurrent feature in these measurements is the appearance of a double-peak, at short times (for example, at t≈1.5μs in Figure 2b). Immediately following coalescence, numerous normal modes will contribute to the shape of the droplet, and their analysis is neglected for the current purposes focussing instead on reproducing the longer time decaying amplitude. However, it is clear that the double peak arises when the deformation of the droplet is such that the parameter δ briefly traverses the crest of one of the high intensity ridges before returning to smaller deformations, as shown by the inset of Figure 2a. This feature may be qualitatively recreated by fitting low order modes to it, neglecting the long time dependence, as shown in Figure S2. However, beyond this region of interest the simulation diverges from the experimental data. As remarked above, the early time behaviour will involve many normal modes and Figure S2 is included to illustrate that fitting early time data may be fraught with ambiguity until such time as the higher order modes have decayed. From equation (2) in the manuscript, the decay times for l=2, 3, 4, 5 and 6 are 4.65, 1.66, 0.86, 0.53 and 0.36 μs, respectively, for an aqueous sodium chloride droplet with a solute concentration of 1.3 M, a surface tension of 73.8 mN m^{-1} and a viscosity of 1.1 mPa s.

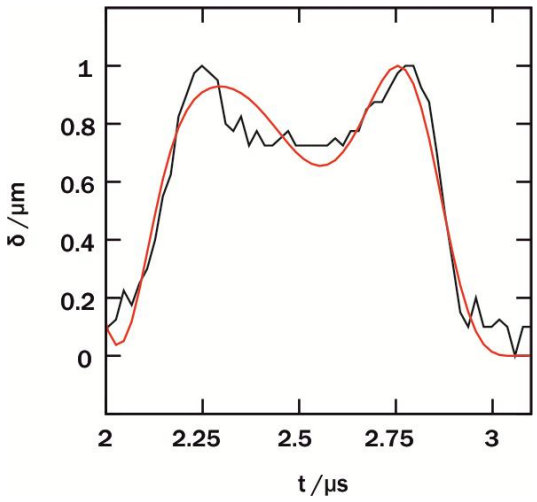

Figure S2: The double peak in the measured back scatter intensity is a frequently observed feature in the time-variation of the scattering intensity occurring shortly after droplet coalescence.

Measurement of the Binary Coalescence Time, τ

While the oscillatory behaviour of droplets in the underdamped regime has been studied in Figure 2, the non-periodic decay has also been studied at higher viscosities. (η>0.01 Pa s) The amplitude of the distortion decays with a time constant for the *l*-th order mode as given by Chandrasekhar, [33] equation (1) in the main paper. ADDEM [43,44] is used to model the surface tension for sucrose and sodium chloride aerosol as well as their mixtures. Approximating the measured damping time to that of the dominant *l*=2 mode allows measurement of viscosity. As shown in figure 1 we have used three methods to measure this damping time and the methods for estimating the binary coalescence time, τ, are described below.

1. Measurements of τ from the decay of back scattered light

The characteristic time for the binary coalescence process is calculated by fitting an exponential decay to the time-resolved light scattering signal as shown in Figure S3.

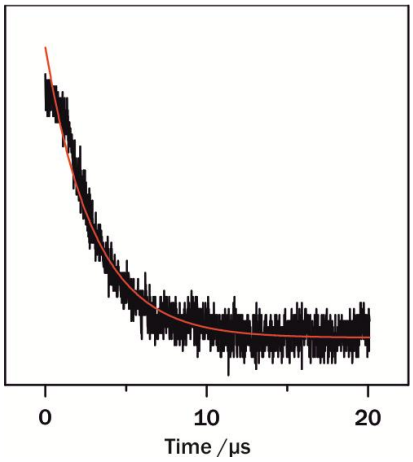

Figure S3: Measurement of the characteristic time for binary coalescence between two pairs of sucrose particles at 74.2% RH with a corresponding damping time of 3 ± 0.032 μs.

2. Measurements of τ using high-frame rate brightfield imaging

The exponential behaviour of the damped oscillation can be seen in the brightfield image and can be closely approximated by the eccentricity of the composite droplet; this can be measured from the brightfield image as shown in Figure S4.

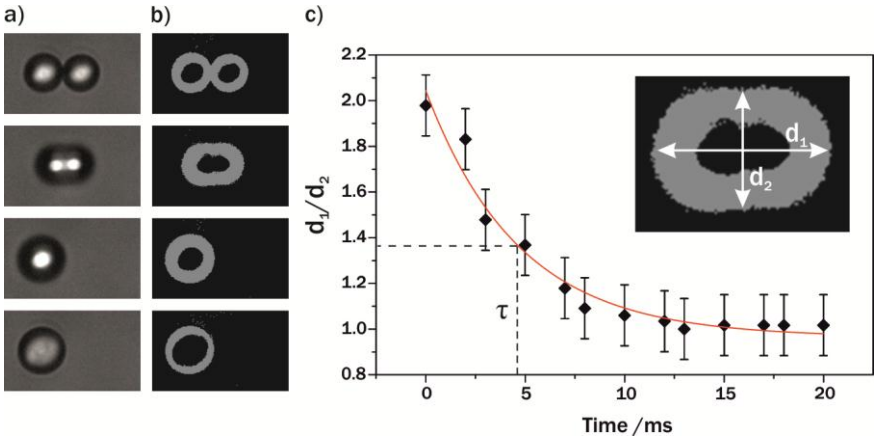

Figure S4: Measurement of the characteristic timescale for binary coalescence between two sucrose particles held at 65% RH by brightfield imaging. (a) Non-consecutive images recorded at 588 Hz showing capillary driven relaxation. (b) A low light intensity threshold is applied to the image, reducing each image to a binary map, allowing measurement of the major and minor axes of the droplet, d_1 and d_2 respectively. (c) An exponential fit to the ratio between these axes provides a measurement of the damping time, τ. In this case, τ=4.68 ± 0.469 ms. Error bars arise from the uncertainty in resolving the droplet boundary based on an error of ±4 pixels in a typical droplet of 60 pixels diameter.

3. Measurements of τ using cavity enhanced Raman scattering

The presence of whispering gallery modes in the Raman spectrum can be used as a probe of the droplet shape. The condition for the droplet to act as an optical resonator has been explored in some detail for

spherical particles [45] however for the non-spherical composites observed during relaxation the precise geometries are less well understood. However, a high degree of sphericity is required in the composite droplet to support whispering gallery modes, allowing a semi-empirical method to be used to measure the damping time using CERS. The mode loss following coalescence and the subsequent mode return are measured using a threshold based peak fitting algorithm. The Raman scattering signal and brightfield image can be measured simultaneously allowing calibration of the mode loss and return times with respect to τ determined from the brightfield imaging. The calibration was performed using 10 droplet pairs and the relationship between τ and the measured time from CERS is given by:

$$\tau = n(\tau_{CERS})$$

For mode loss n=3.21 ± 0.58, while for full mode return n=0.17 ± 0.06. Then, a coalescence time equivalent to that determined from the brightfield imaging can be estimated. Monitoring the mode then allows measurements to be made at much higher viscosities than can be accessed by observing changes in deformation in the brightfield image.

Thermodynamic modelling of sucrose solutions with variation in water activity

The ability of three commonly used thermodynamic models to predict the equilibrium composition of aqueous sucrose and sucrose/sodium chloride solutions was tested by comparison of predicted viscosities based on these thermodynamic relationships with experimental data. The three treatments considered have been described and assessed in detail in a previous publication and we only briefly review their use here. [48]

The thermodynamic treatment used in the aerosol modelling tool ADDEM [44,49] (aerosol diameter dependent equilibrium model) for the water activity of mixtures containing both organic and inorganic solutes is based on the semi-empirical UNIFAC system. The equilibrium size of an aqueous droplet is calculated by an iterative method, solving the Köhler equation and accounting for both the solute and Kelvin effects. The equilibrium droplet size and *RH* are related by:

$$RH = a_w exp\left(\frac{2V_w\sigma}{RTR_p}\right)$$

where a_w is the activity of water in an equivalent bulk solution, V_w is the partial molar volume of water, σ is surface tension, R_p is the radius of the liquid droplet and R and T are the ideal gas constant and the temperature.

Starzak & Peacock provided a fit to experimental data using the Margules equation to calculate the activity coefficient γ_w allowing the water activity to be estimated for a specific mole fraction of solute. [50]

$$ln\gamma_w = \frac{Q}{RT}(x_s^0)^2[1 + b_1x_s^0 + b_2(x_s^0)^2]$$

where x_s^0 is the nominal mole fraction of sucrose, Q = -17538 Jmol^{-1}, b_1 = -1.0038 and b_2 = -0.24653. In this treatment, and the following one, no correction for surface curvature was made: the particle sizes are considerably larger than 1 μm and it can be assumed in this limit that a_w=RH.

Norrish related water activity of nonelectrolyte solutions to the mole fractions of water and solute, x_w and x_s respectively. [51]

$$a_w = x_w \exp(k x_s^2)$$

where k is an empirically determined parameter and is -6.47 for sucrose.

Modelling the viscosity of binary sucrose solutions

The kinematic viscosity (v) of binary sucrose solutions of molalities from 10^{-2} to 10^2 mol kg^{-1} has been modelled using the model proposed by Chenlo et al. [52] Using predictions from ADDEM for the solution density, which uses a volume additivity approach, [48] the dynamic viscosity can be calculated from:

$$\frac{v}{v_w} = 1 + am \exp\left(\frac{m^c}{d(T_R)^3 - 1.001}\right)$$

$$T_R = \frac{T(K)}{273.15}$$

where v_w is the kinematic viscosity of water, m is the molality of sucrose, and a, c and d are empirically determined parameters provided by Chenlo et al. [42]

Modelling the viscosity of ternary sucrose/sodium chloride solutions

The equilibrium compositions of sucrose and sodium chloride solutions have been modelled using the Norrish and ADDEM models, respectively. As can be seen in Figure 3a, the Norrish treatment best fits the experimental data for binary sucrose solutions, while the ADDEM model, based on the equations of Clegg et al., [53] has been shown previously to predict the water activity of sodium chloride solutions to a high degree of accuracy. [54] For the mixture, the Zdanovskii-Stokes-Robinson (ZSR) relationship [55] states that for a specific water activity the total water content W_{total} of a solution droplet containing multiple dissolved solutes can be expressed as the sum of the amounts of water associated with each component:

$$W_{total} = \sum_i w_i^0$$

where w_i^0 is the water associated with component i.

The kinematic viscosity of sucrose/sodium chloride droplets of varying stoichiometries have been modelled using the ZSR relationship and the model proposed by Chenlo et al. for ternary sucrose/sodium chloride solutions [56]. Using predictions from ADDEM for the solution density the dynamic viscosity was calculated.

$$\frac{\upsilon}{\upsilon_w} = 1 + \sum_{i=1}^{2} \Psi_i + \omega(T_R) \prod_{i=1}^{2} (jm \exp(km^n)_i$$

$$\omega(T_R) = \exp(-3.737T_R^2)$$

$$\Psi = em\ exp\left(\frac{m^f}{gT_R + h}\right)$$

Where m is the molality of sucrose or sodium chloride and f, g, h, j, k and n are empirically determined parameters. [42]

For comparison, the viscosity of the unmixed components was modelled in the same way and the viscosity of the mixture calculated using the commonly used Refutas equation, based on the viscosity blending index (VBI) of the two components. [57]

$$\upsilon_{Blend} = 10^{-6}\exp\left(\exp\left(\frac{VBI_{Blend} - 10.975}{14.535}\right)\right)$$

$$VBI_{Blend} = \sum_{i=1}^{N} f_i VBI_i$$

$$VBI_i = 14.354 \ln(\ln(\upsilon_i + 0.8)) + 10.975$$

As shown in Figure S7, this treatment is particularly poor at reproducing the experimental trends and has been omitted from Figure 3b for clarity.

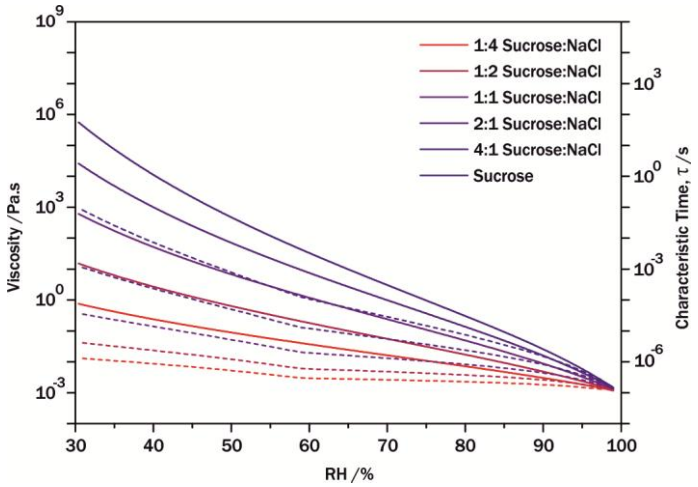

Figure S6: Viscosity of sucrose/sodium chloride solutions calculated from: (i) the Chenlo parameterisation using the thermodynamic treatments of Norrish and ADDEM respectively and mixing based on ZSR – solid lines; (ii) unmixed components treated using Chenlo with mixing based on Refutas – dashed lines. While the former treatment, as shown in Fig 3b, under predicts the measured viscosities by 1-2 orders of magnitude, the Refutas treatment gives poorer agreement, under predicting viscosity by almost 3 orders of magnitude for the highest sucrose concentrations.

Validation of viscosity measurements

Validation of the viscosity measurements has been demonstrated in the dilute solution limit for NaCl through the agreement between the measurements of Chenlo et al. under sub-saturated conditions and the measurements made of the damped periodic decay in droplet shape as in Figure 3a). The measured viscosities of two viscous solvents, glycerol and 1,2,6-hexanetriol allow validation at intermediate viscosities in the aperiodic regime as show in Figure S5.

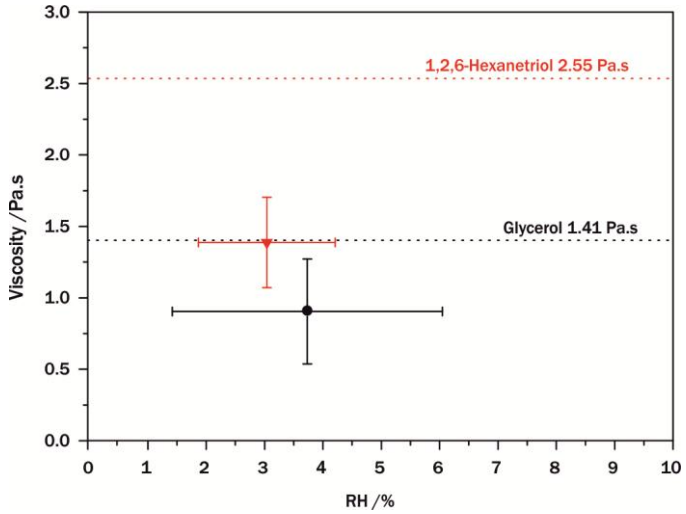

Figure S5: Measurements of viscosity for glycerol (black circle) and 1,2,6-hexanetriol (red triangle) droplets. The damping time was measured using elastic light scattering in the overdamped regime (η>0.01 Pa s) for 3 and 5 separate coalescence events respectively, error bars correspond to standard deviations in both the measured RH and viscosity. The measurements show a good agreement with known values [46,47] for these compounds to within a factor of 2.

Due to the difficulty of aerosolising standards of higher viscosity which are not water soluble, validation against compounds of higher known viscosity has not been possible. However comparison between the experimental data and the model of Quintas et al.[58], valid for $0.54 < a_w < 0.77$, shows good agreement providing validation up to ~10^4 Pa.s. It should be noted that the Quintas model based on the WLF (Williams, Landel, Ferry) treatment[59] is only valid at higher water activities (above saturation) and as such the Chenlo model has been used throughout the rest of the paper for comparison with experimental data.

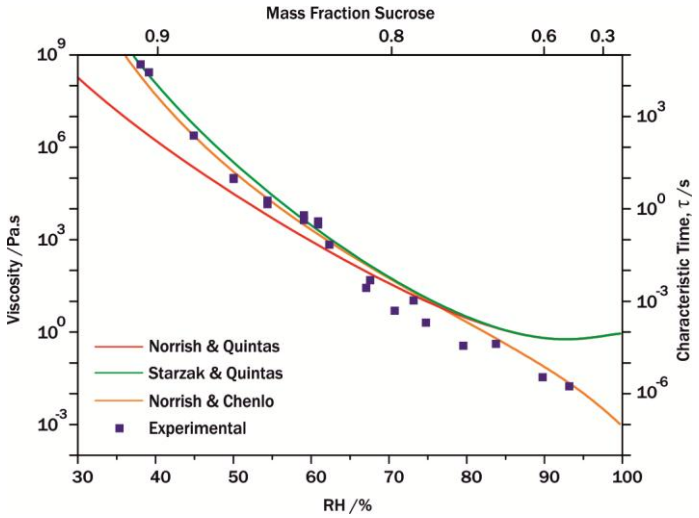

Figure S6: Comparison between the experimental measurements of sucrose viscosity from Figure 3a) and the model of Quintas et al. using both the Norrish and Starzak treatments for water activity. The Chenlo model using the Norrish treatment which has been found to best represent the experimental data has been included. The Quintas model shows good agreement with the experimental data for $0.54 < a_w < 0.77$, the range over which this particular model is valid.

REFERENCES

31 Suryanarayana, P. V. R. & Bayazitoglu, Y. Surface tension and viscosity from damped free oscillations of viscous droplets. *International Journal of Thermophysics* **12**, 137-151 (1991).

32 Miller, C. A. & Scriven, L. E. The oscillations of a fluid droplet immersed in another fluid. *Journal of Fluid Mechanics* **32**, 417-435 (1968).

33 Chandrasekhar, S. *Hydrodynamic and Hydromagnetic Stability*. (Dover, 1961).

34 Kahnert, F. M. Numerical methods in electromagnetic scattering theory (Reprinted from vol 79, pg 775-824, 2003). *Journal of Quantitative Spectroscopy & Radiative Transfer* **111**, 1791-1840 (2010).

35 Mishchenko MI, T. L., Lacis AA. *Scattering, absorption, and emission of light by small particles.*, (Cambridge University press, 2002).

36 Wiscombe, W. J. Improved Mie scattering algorithms. *Appl. Opt.* **19**, 1505-1509 (1980).

37 Lock, J. A. & Gouesbet, G. Rigorous justification of the localized approximation to the beam-shape coefficients in generalized Lorenz-Mie theory. *Journal of the Optical Society of America a-Optics Image Science and Vision* **11**, 2503-2515 (1994).

38 Yamada, T. & Sakai, K. Observation of collision and oscillation of microdroplets with extremely large shear deformation. *Physics of Fluids* **24** (2012).

39 Born M, W. E. *Principles of optics: electromagnetic theory of propagation, interference and diffraction of light.*, (Cambridge University press, 1999).

40 Miles, R. E. H., Walker, J. S., Burnham, D. R. & Reid, J. P. Retrieval of the complex refractive index of aerosol droplets from optical tweezers measurements. *Physical Chemistry Chemical Physics* **14**, 3037-3047 (2012).

41 Tang, I. N. Thermodynamic and optical properties of mixed-salt aerosols of atmospheric importance. *Journal of Geophysical Research-Atmospheres* **102**, 1883-1893 (1997).

42 Chenlo, F., Moreira, R., Pereira, G. & Ampudia, A. Viscosities of aqueous solutions of sucrose and sodium chloride of interest in osmotic dehydration processes. *Journal of Food Engineering* **54**, 347-352 (2002).

43 Topping, D. O., McFiggans, G. B. & Coe, H. A curved multi-component aerosol hygroscopicity model framework: Part 1 - Inorganic compounds. *Atmospheric Chemistry and Physics* **5**, 1205-1222 (2005).

44 Topping, D. O., McFiggans, G. B. & Coe, H. A curved multi-component aerosol hygroscopicity model framework: Part 2 - Including organic compounds. *Atmospheric Chemistry and Physics* **5**, 1223-1242 (2005).
45 Chen, G., Chang, R. K., Hill, S. C. & Barber, P. W. Frequency splitting of degenerate spherical cavity modes - stimulated Raman-scattering spectrum of deformed droplets. *Optics Letters* **16**, 1269-1271 (1991).
46 Segur, J. B. & Oberstar, H. E. Viscosity of glycerol and its aqueous solutions. *Industrial and Engineering Chemistry* **43**, 2117-2120 (1951).
47 Flick, I. *Industrial Solvents Handbook, 5th Edition*. (Noyes Publications, 1998).
48 Tong, H. J., Reid, J. P., Bones, D. L., Luo, B. P. & Krieger, U. K. Measurements of the timescales for the mass transfer of water in glassy aerosol at low relative humidity and ambient temperature. *Atmospheric Chemistry and Physics* **11**, 4739-4754 (2011).
49 Topping, McFiggans & Coe. A curved multi-component aerosol hygroscopicity model framework: part 1 - inorganic compounds. *Atmosheric chemistry and physics* **5**, 1205-1222 (2005).
50 Starzak, M. & Peacock, S. D. Water activity coefficient in aqueous solutions of sucrose - A comprehensive data analysis. *Zuckerindustrie* **122**, 380-387 (1997).
51 Norrish, R. S. An equation for the activity coefficients and equilibrium relative humidities of water in confectionary syrups. *Journal of Food Technology* **1**, 25-39 (1966).
52 Chenlo, F., Moreira, R., Pereira, G. & Ampudia. A. Viscosities of aqueous solutions of sucrose and sodium chloride of interest in osmotic dehydration processes. *Journal of Food Engineering* **54**, 347-352 (2002).
53 Clegg, S. L., Brimblecombe, P. & Wexler, A. S. Thermodynamic model of the system H+-NH4+-Na+-SO42--NB3--Cl--H2O at 298.15 K. *Journal of Physical Chemistry A* **102**, 2155-2171 (1998).
54 Hanford, K. Mitchem, L., Reid, J.P., Clegg, S.L., Topping, D.O., *et al.* Comparative thermodynamic studies of aqueous glutaric acid, ammonium sulfate and sodium chloride aerosol at high humidity. *Journal of Physical Chemistry A* **112**, 9413-9422 (2008).
55 Stokes, R. H. & Robinson, R. A. Interactions in aqueous nonelectrolye solutions I. Solute-solvent equilibria. *Journal of Physical Chemistry* **70**, 2126-& (1966).
56 Chenlo, F., Moreira, R., Pereira, G. & Bello. P. An equation for modelling the kinematic viscosities of binary and ternary solutions with sugars and sodium chloride as a function of concentration and temperature experimental data of solutions with lactose. *International Journal of Food Properties* **9**, 149-156 (2006).
57 Barabas, I. & Todorut, I. A. Predicting the Temperature Dependent Viscosity of Biodiesel-Diesel-Bioethanol Blends. *Energy & Fuels* **25**, 5767-5774 (2011).
58 Quintas, M., Brandao, T. R. S., Silva, C. L. M. & Cunha, R.L. Rheology of supersaturated sucrose solutions. *Journal of Food Engineering*, 2006, **77**(4), 844-852.
59 Williams, M.L , Landel, R.F, Ferry, J.D, The temperature dependence of relaxation mechanisms in amorphous polymers and other glass-forming liquids. *J.Am. Chem. Soc.* **77**, 3701-3707 (1955).